

Persistent homology and topological statistics of hyperuniform point clouds

Marco Salvalaglio,^{1,2,*} Dominic J. Skinner,³ Jörn Dunkel,⁴ and Axel Voigt^{1,2,5}

¹*Institute of Scientific Computing, Technische Universität Dresden, 01062 Dresden, Germany*

²*Dresden Center for Computational Materials Science (DCMS), TU Dresden, 01062 Dresden, Germany*

³*NSF-Simons Center for Quantitative Biology, Northwestern University, 2205 Tech Drive, Evanston, IL 60208, USA*

⁴*Department of Mathematics, Massachusetts Institute of Technology,
77 Massachusetts Avenue, Cambridge, MA 01239, USA*

⁵*Cluster of Excellence Physics of Life, Technische Universität Dresden, 01062 Dresden, Germany*

(Dated: March 26, 2024)

Hyperuniformity, the suppression of density fluctuations at large length scales, is observed across a wide variety of domains, from cosmology to condensed matter and biological systems. Although the standard definition of hyperuniformity only utilizes information at the largest scales, hyperuniform configurations have distinctive local characteristics. However, the influence of global hyperuniformity on local structure has remained largely unexplored; establishing this connection can help uncover long-range interaction mechanisms and detect hyperuniform traits in finite-size systems. Here, we study the topological properties of hyperuniform point clouds by characterizing their persistent homology and the statistics of local graph neighborhoods. We find that varying the structure factor results in configurations with systematically different topological properties. Moreover, these topological properties are conserved for subsets of hyperuniform point clouds, establishing a connection between finite-sized systems and idealized reference arrangements. Comparing distributions of local topological neighborhoods reveals that the hyperuniform arrangements lie along a primarily one-dimensional manifold reflecting an order-to-disorder transition via hyperuniform configurations. The results presented here complement existing characterizations of hyperuniform phases of matter, and they show how local topological features can be used to detect hyperuniformity in size-limited simulations and experiments.

I. INTRODUCTION

Hyperuniform (HU) systems are characterized by vanishing density fluctuations at large length scales [1]. This property is trivially present in ordered systems, whereas for disordered systems it realizes a distinguishable state of matter [2] lying between (quasi)-crystalline and amorphous or liquid phases: HU systems feature long-range order while being statistically isotropic with no Bragg peaks. These systems can exist either as equilibrium or quenched nonequilibrium phases and exhibit a range of peculiar electronic, photonic, or other transport properties [2, 3]. HU arrangements emerge in diffusive systems [4, 5], emulsions [6], amorphous materials [7], nanostructure self-assembly [8], supercooled liquid and glasses [9–11], vortexes in superconductors [12–14], avian photoreceptors [15], swimmers [16], and cosmology [17, 18] (for which it was first termed *superhomogeneity*). Systems engineered to be HU have found many applications, including polarization sensitivity [19], lasing [20, 21], coatings with unusual anti-reflective properties or appearance [22, 23] and full photonic band gaps for light propagation [19, 24, 25] within optics, as well as topologically protected electronic states [26] and mechanical systems [27]. HU patterns also attract significant attention from statistics and probability theory [28–30].

Proper analysis of HU patterns is necessary for thorough explorations and detection of their distinctive prop-

erties. Although it has become straightforward to generate HU point patterns [31–34], the identification and characterization of HU patterns in both experimental systems and numerical simulation frameworks remains challenging: HU characteristics are only rigorously defined for infinitely large systems [2], whereas any experimental or simulated data set is finite in size, and often only contains hundreds of points, see for instance [10–13]. Consequently, their characterization is based on empirical diagnostics, essentially extrapolating measurements from finite length scales to infinity. Recent analyses have improved this statistical estimation [35]. However, an ideal HU character may be lost due to the presence of defects or perturbations even in strongly correlated systems [36–38], although the corresponding pattern should retain some essential properties of the ideal HU arrangements. In brief, HU patterns exhibit local structures that we would like to characterize and explore in finite systems, aside from infinite wavelength measurements. Here, we pursue a topological approach, which by its nature, is robust to small changes in the system, providing an orthogonal way to characterize and explore HU structure without estimating global properties directly.

Specifically, we aim to characterize HU point configurations by applying methods from topological data analysis (TDA). The TDA framework employs techniques from algebraic topology to extract and analyze structures from complex datasets [39]. A method of particular interest to our study is *persistent homology* [40–42], which enables the robust and compact characterization of topological features across multiple scales for point clouds and other discrete data [43]. Practical computational methods have

* marco.salvalaglio@tu-dresden.de

been developed to implement persistent homology calculations, and these tools have been applied across a range of disciplines [44, 45]. Furthermore, we will also investigate the statistics of local topological neighborhoods in HU point patterns derived from the Delaunay tessellation [46, 47], using a recently introduced framework [48, 49]. The Delaunay tessellation characterizes the topological neighborhood structure, and whilst it will be different for each specific realization, we can robustly quantify its statistical properties, essentially counting how frequently each local topological neighborhood motif occurs in a point pattern. As these neighborhoods only change through discrete topological transitions, counting the number of transitions needed to transform one system into another gives a measure of the distance between HU systems [48, 49]. Altogether, our results demonstrate that topological approaches can provide robust characterizations of HU configurations, even for finite systems.

The paper is organized as follows. In Sec. II, we briefly review the basic notions of HU systems and describe the generation and parametrization of point clouds. In Sec. III we study the persistent homology of these patterns, quantifying differences and similarities between patterns. We also investigate how the underlying HU character can be detected in subsets of generated HU configurations. Sec. IV analyzes the statistics of local graph neighborhoods, which enables comparisons between HU configurations. We find that many different HU configurations lie on a primarily one-dimensional manifold reflecting an order-to-disorder transition. The main conclusions are summarized in Sec. V.

II. HYPERUNIFORMITY AND GENERATION OF POINT CLOUDS

An arrangement of points in a d -dimensional Euclidean space is said to be HU if the variance $\sigma_N^2(R)$ of the number of points in a d -dimensional spherical observation window with radius R scales slower than the volume of this window [1],

$$\lim_{R \rightarrow \infty} \frac{\sigma_N^2(R)}{R^d} = 0. \quad (1)$$

Rather than work with the variance directly, it is equivalent, and often easier, to define hyperuniformity in terms of the structure factor for an N particle system [2]

$$S(\mathbf{k}, \{\mathbf{r}_j\}) = \frac{1}{N} \left| \sum_{j=1}^N \exp(i\mathbf{k} \cdot \mathbf{r}_j) \right|^2, \quad (2)$$

with \mathbf{r}_j the position of particle j , and \mathbf{k} a wave vector. Formally, we only define $S(\mathbf{k}, \{\mathbf{r}_j\})$ at a finite number of $\mathbf{k} = (k_1, \dots, k_d)$ vectors with components $k_i = 2\pi n/L_i$, confining our particles in a d -dimensional box with side lengths L_i . In the $N \rightarrow \infty$ limit, $S(\mathbf{k}, \{\mathbf{r}_j\})$, simply referred to as $S(\mathbf{k})$ hereafter, becomes a continuous function of \mathbf{k} , aside from a formal singularity at $\mathbf{k} = \mathbf{0}$ (note

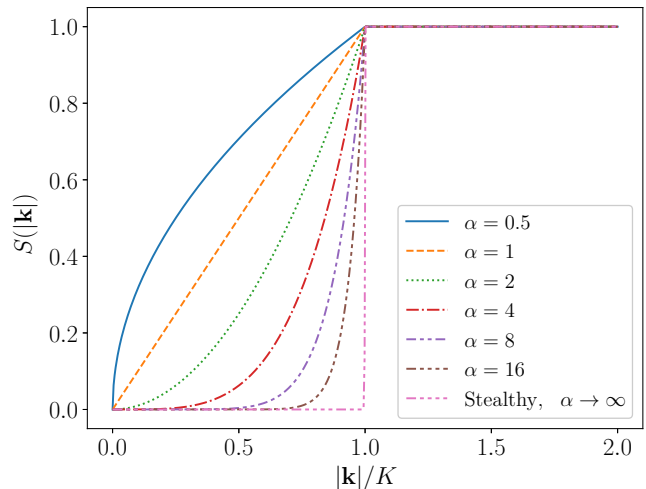


FIG. 1. The parameterized structure factor $S_0(|\mathbf{k}|)$ from Eq. (6) for different α and $H = 0$, showing hyperuniformity ($S(|\mathbf{k}|) \rightarrow 0$ as $\mathbf{k} \rightarrow 0$).

$S(\mathbf{0}) = N$) [2]. Having taken this limit, a definition of a HU system equivalent to (1) is [2]

$$\lim_{|\mathbf{k}| \rightarrow 0} S(\mathbf{k}) = 0. \quad (3)$$

Both conditions (1) and (3) can be realized with different scalings of $\sigma_N^2(R)$ and $S(\mathbf{k})$. For systems characterized by a power law $S(\mathbf{k}) = |\mathbf{k}|^\alpha$ with $\alpha > 0$ for $|\mathbf{k}| \rightarrow 0$, three characteristic scaling behaviors are realized, namely

$$\sigma_N^2(R) \sim \begin{cases} R^{d-1} & \alpha > 1 \\ R^{d-1} \ln(R) & \alpha = 1 \\ R^{d-\alpha} & 0 < \alpha < 1 \end{cases}, \quad (4)$$

with these three conditions referred to as HU classes I, II, and III, respectively [2].

Point clouds with a prescribed structure factor, $S_0(\mathbf{k})$, can be generated by solving an optimization problem [31, 32]. In short, from an initial N -point arrangement with position of points $\{\mathbf{r}_j\}$ given, minimize an objective function,

$$F(\{\mathbf{r}_j\}) = \sum_{\mathbf{k}} |S(\mathbf{k}) - S_0(\mathbf{k})|^2, \quad (5)$$

resulting in a least-square problem, where the sum over \mathbf{k} is taken over wave vectors appropriate for the finite-size bounding box. The minimization can be performed with standard algorithms like the conjugate-gradient, Broyden-Fletcher-Goldfarb-Shanno, or dogleg algorithms [31, 32].

We consider here a tunable, prototypical form for a power-law behavior of S_0 as follows (see also Fig. 1)

$$S_0(\mathbf{k}) = \begin{cases} D(1-H)|\mathbf{k}|^\alpha + H & |\mathbf{k}| < K, \\ 1 & \text{otherwise,} \end{cases} \quad (6)$$

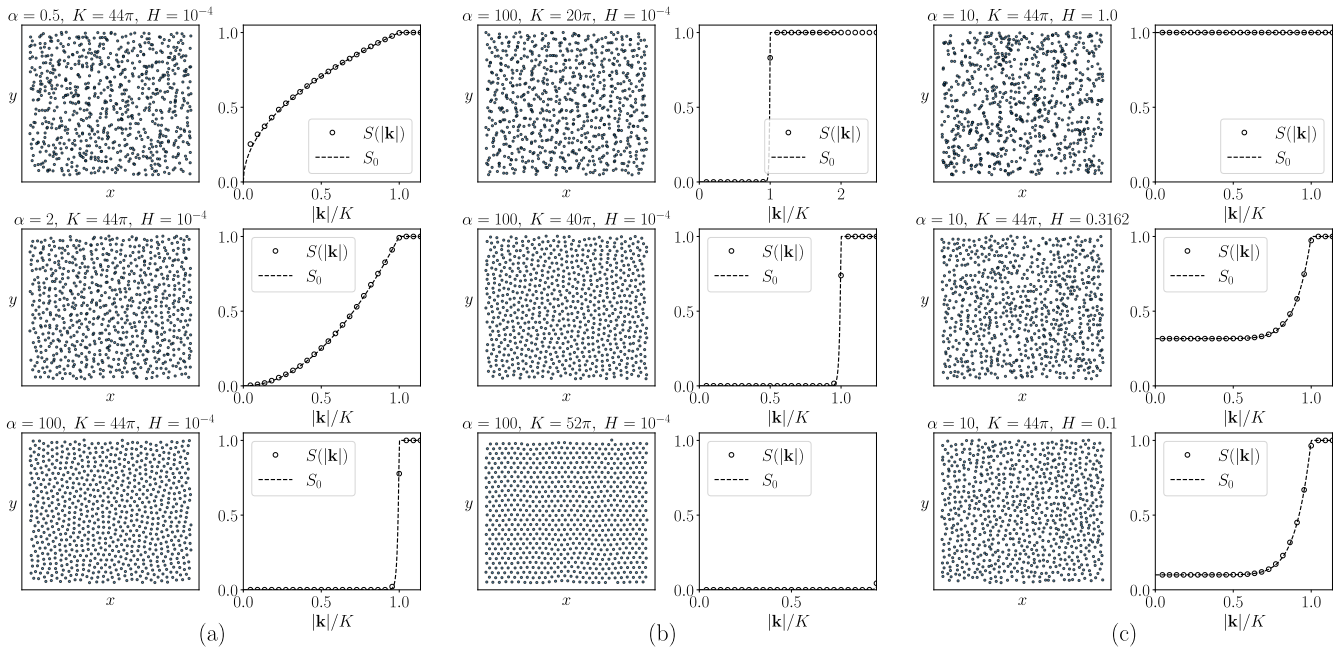


FIG. 2. Examples of HU and non-HU point patterns ($N = 780$) generated as described in Sec. II, shown together with the radial average of the structure factor $S(|\mathbf{k}|)$ and the target structure factor, S_0 . (a) $K = 44\pi$, $H = 10^{-4}$ with $\alpha = 0.5, 2$ and 100 from top to bottom. For $\alpha = 100$ an effective stealthy HU point cloud is obtained. (b) $\alpha = 100$, $H = 10^{-4}$ with $K = 20\pi, 40\pi$ and 52π from top to bottom. These are all stealthy HU point clouds and the order-disorder transition is expected for $K \approx 45\pi$. Note that for $K = 52\pi$ a slightly perturbed triangular lattice is obtained. (c) $\alpha = 100$, $K = 40\pi$, with $H = 1.0, 0.3162$ and 0.1 from top to bottom. $S(|\mathbf{k}|)$ is shown for the same range of $|\mathbf{k}|$ ($|\mathbf{k}| \in [0, 52\pi]$) in all the plots.

with $D = K^{-\alpha}$ and H, K , and α three parameters controlling specific pattern features as detailed below.

The scaling exponent α controls the class of HU as defined in Eq. (4), and thus the overall shape of the structure factor, Fig. 1. The limit of large α gives a finite-size region with $S(\mathbf{k}) = H$, a feature referred to as *stealthy hyperuniformity* for $H \approx 0$ (see Fig. 2a, with a stealthy HU point cloud effectively obtained for $\alpha = 100$ and $H = 10^{-4}$).

Loosely speaking, K sets the length scale, $2\pi/K$, above which correlations are enforced in the system. A small K only suppresses fluctuations on the largest scales, allowing for more locally disordered arrangements whereas a large K constrains arrangements at the size of a typical neighborhood. For stealthy HU configurations ($S(\mathbf{k}) \sim 0$ for $0 < |\mathbf{k}| \leq K$), a known transition from disordered to ordered systems, signaled by the emergence of Bragg peaks in $S(\mathbf{k})$, is obtained at [2, 50]

$$K = c_d \rho^{1/d}, \quad (7)$$

where $\rho = N/V$ is the density, d the system dimensionality, and c_d a (known) constant. In 2D, for $V = 1$, stealthy HU disordered configurations are obtained for $K < \sqrt{8\pi N}$ (see also Fig. 2b, for which $\sqrt{8\pi N} \approx 45\pi$).

The parameterization in (6) is chosen so that $H = \tilde{H}$,

where

$$\tilde{H}[S] = \lim_{|\mathbf{k}| \rightarrow 0} \frac{S(|\mathbf{k}|)}{S(k_{\max})}, \quad (8)$$

with k_{\max} the characteristic wavenumber at which $S(\mathbf{k})$ assumes its maximum value. Formally, $\tilde{H} = 0$ for HU patterns (Eq. (3)), although for finite-size systems \tilde{H} cannot be directly evaluated and must be extrapolated, as $|\mathbf{k}| \rightarrow 0$ implies a system with infinite size [2, 8]. Moreover, this quantity may deviate from zero due to the presence of defects or data artifacts (e.g., in experimental images). A commonly accepted convention is to say a point pattern is *nearly* HU for $\tilde{H} \leq 10^{-2}$ and *effectively* HU for $\tilde{H} \leq 10^{-4}$ [51, 52]. By tuning the parameter H , we can study the convergence to HU, and how that alters the topology of the patterns (see also Fig. 2c).

In the following, we will consider $d = 2$ space dimensions and generate point patterns for $N = 780$ in a square 2D domain with unitary sides, as illustrated in Fig. 2. N is chosen such that the points can be arranged almost as an ideal triangular arrangement (closest packing in 2D). Such a lattice can be obtained by arranging $2q$ rows of p particles with p/q a close approximation of $\sqrt{3}$. A set of possible p, q choices is reported in [31]. We obtain pat-

terns by varying parameters in the following ranges

$$\begin{aligned} H &\in [10^{-4}, 1], \\ \alpha &\in [0.5, 100], \\ K &\in [20\pi, 56\pi]. \end{aligned} \quad (9)$$

We generated 880 patterns by varying the parameters in the range shown in Eq. (9). All combinations start from a periodic point pattern with relatively small random noise before minimizing F [31, 32], with ten different random seeds, and hence ten final patterns for each parameter combination.

Examples of generated patterns, with varying K , α , and H parameter values, are shown in Fig. 2 together with the radial average of the structure factor, $S(|\mathbf{k}|)$, and the target structure factor S_0 . Varying α for a small H (effective HU) and a fixed K close to the nominal order-disorder transition for stealthy HU patterns explores the three different HU classes from Eq. (4), where increasing α leads to more and more uniformly distributed points (Fig. 2, first column). A qualitatively similar effect is observed by varying K (Fig. 2, second column). For small K , even a stealthy HU configuration leads to small-scale agglomerates because no correlation is imposed for length scales smaller than $2\pi/K$. Approaching the order-disorder transition leads to a more uniform arrangement, while above the critical point, a (slightly perturbed) triangular arrangement is obtained. The effect of H is illustrated first in the limiting case of $H = 1$, resulting in a random point pattern, and for two other values (Fig. 2, third column) showing the impact of lowering the small wave vector limit of S (still far from a nearly HU pattern). Although the trends appear clear, it remains challenging to quantify differences and similarities between these patterns, particularly when far away from limiting cases (random or ordered). In the remainder, we show how one can overcome this problem by studying and characterizing the topology of these point patterns.

III. PERSISTENT HOMOLOGY

Persistent homology [40–42] uses ideas from algebraic topology to understand the “shape” of a data set, building on how homology characterizes geometric objects through connected components, loops, and voids (Betti numbers). Starting from a point set P , persistent homology constructs a family of simplicial complexes (collection of points, lines, triangles, tetrahedrons, and higher dimensional analogs), K_P^l , parameterized by $r \geq 0$, such that $K_P^l \subseteq K_P^m$ for $l < m$. This nested family of simplicial complexes is called a *filtration*. Persistent homology takes the appearance (*birth*) and disappearance (*death*) of homological features of this filtration, as r is varied, as the essential topological information that characterizes the point set. A graphical representation for the births and deaths of topological features in the filtration is called the *persistence diagram* [44, 45, 53], see Fig. 3, which is discussed further below.

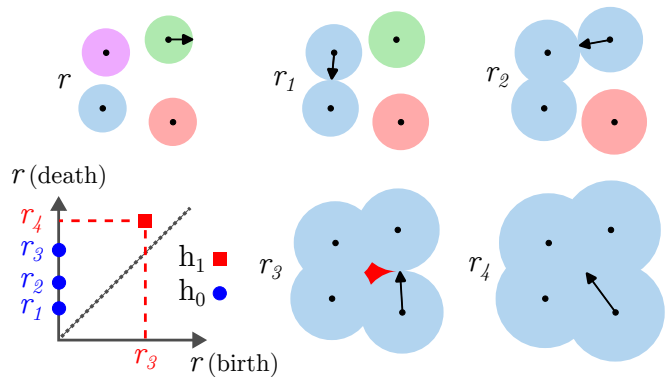


FIG. 3. Illustration of the persistence diagram (bottom left) for a four-point arrangement (top left), and a family of nested Vietoris-Rips complexes. We parameterize the complex by r , where r is the radius (*time*) of circles centered on the points. Shown are radii, r_i , at which features are added to the persistence diagram. Blue points on the persistence diagram represent the birth/death of h_0 , or connected components, including initial isolated circles which all have a birth time of 0, and death times of $r_{1,2,3}$. The red square represents h_1 , the hole (or closed loop) within the domains, forming at r_3 and vanishing at r_4 .

For our choice of filtration, we use the widely adopted Vietoris-Rips complex [42]. In short, consider placing a circle of radius r , which we use as the filtration parameter, around each point in the data set. If two circles overlap, the line connecting the two corresponding points is included in the simplicial complex. In other words, two separated connected components, the points, become one connected component. If three circles all pairwise overlap, then the triangle defined by the three corresponding points is included in the simplicial complex, and so on, see Fig. 3. We increase the radius r , which we hereafter refer to as *time* [44, 45], from zero to infinity, and consider how the resulting topology of the simplicial complex changes. This procedure echoes the concept of diffusion spreadability in a two-phase medium, namely the time-dependent mass transfer from one phase (say, circles) into a second phase (space surrounding the circles) which, interestingly, shows peculiar behaviors for disordered HU configurations [54]. A topological feature, such as a hole, is created at some time and disappears at a later time, Fig. 3. This can be represented as a point on the persistence diagram, with the birth and death times of this feature as the x and y coordinates, respectively. The persistence of a feature is the difference between its death time and birth time, indicating how long the feature exists as the parameter r changes. For our analysis, we will look at the birth/death of connected components, h_0 , and of holes or loops, h_1 (see Fig. 3). In general, h_k generalizes the concept of holes through homology: h_k quantifies k -dimensional holes [42], with zero-dimensional holes then corresponding to connected components and one-dimensional holes corresponding to closed loops or “holes” in an informal sense. Persistent diagrams are

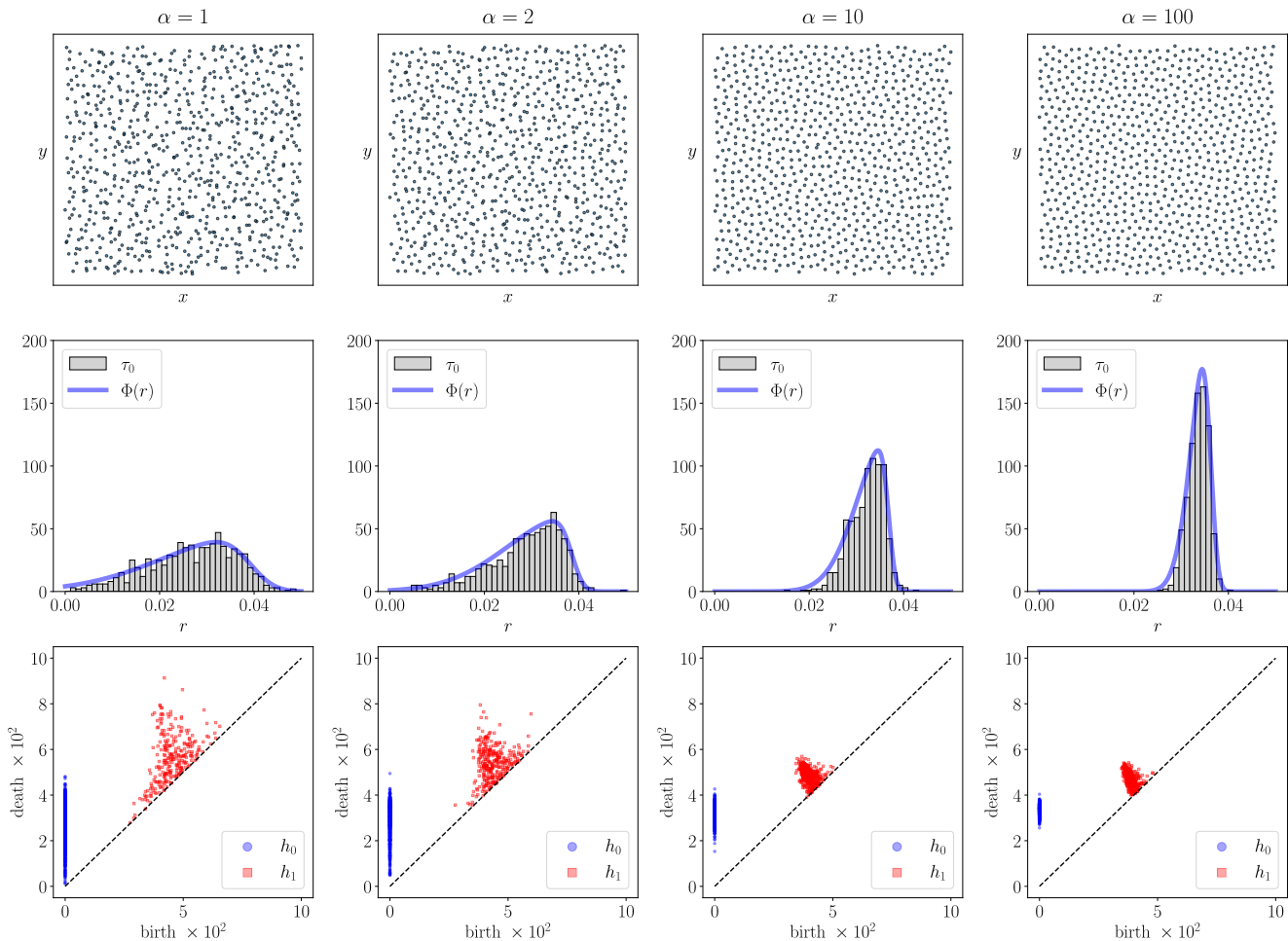


FIG. 4. Persistent homology analysis for representative patterns featuring different α with $K = 44\pi$ and $H = 10^{-4}$. The first row shows four-point patterns. The second row illustrates the death times distribution τ_0 for connected components (h_0) through a histogram and a fit with the skew-normal distribution Φ . The third row shows persistence diagrams for h_0 (connected components) and h_1 (holes). Additional results obtained by varying K and H are reported in the Supplemental Material.

computed using the python library `ripser` [55, 56].

Figure 4 shows persistent homology analysis applied to HU patterns, here obtained by varying α whilst keeping the other parameters constant. Starting from the HU point patterns (first row), we can compute a histogram of death times τ_0 for connected components (second row), and persistence diagrams of connected components, h_0 , and holes, h_1 (third row). The same analysis for patterns obtained by varying K and H is reported in the Supplemental Material. Clear trends emerge, with a narrowing of the distributions for more pronounced HU characters (larger α and K , as well as smaller H). Note that significant variations in the topological features are also observed for patterns that closely resemble each other; cf. $\alpha = 10$ and $\alpha = 100$ in Fig. 4. We find that a skew-normal distribution fits histograms of the death times τ_0 well, see Fig. 4 (second row). Clear trends in the parameters of the skew-normal also emerge when varying α , K , and H , see the Supplemental Material for details.

To quantify differences between patterns from the

topological features obtained above, we use the Wasserstein distance between two persistence diagrams, specifically the distributions of death/birth times for h_0 (connected components) and h_1 (holes). The p -th Wasserstein distance between two persistence diagrams A and B (including the diagonal) is defined as [45]

$$W_p(A, B) = \inf_{\gamma} \left(\sum_{\mathbf{x} \in A} (\|\mathbf{x} - \gamma(\mathbf{x})\|_q)^p \right)^{1/p}, \quad (10)$$

with $\gamma(\mathbf{x})$ ranging over all bijections from A to B and $\|\mathbf{a} - \mathbf{b}\|_q = (\sum_{i=1}^2 |a_i - b_i|^q)^{1/q}$ (as $\mathbf{a}, \mathbf{b} \in \mathbb{R}^2$). Here, q determines the cost of transporting \mathbf{x} to $\gamma(\mathbf{x})$; for example, if $q = 1$, the cost is the L^1 (Manhattan) distance, and if $q = 2$ the cost is the Euclidean distance. Throughout, we set $p = q$. Overall, W_p quantifies the similarities between two sets of points by computing the minimal cost to transform one set of points into another. Calculations involving Wasserstein distances between persistence diagrams used the GUDHI libraries [57]. Other methods

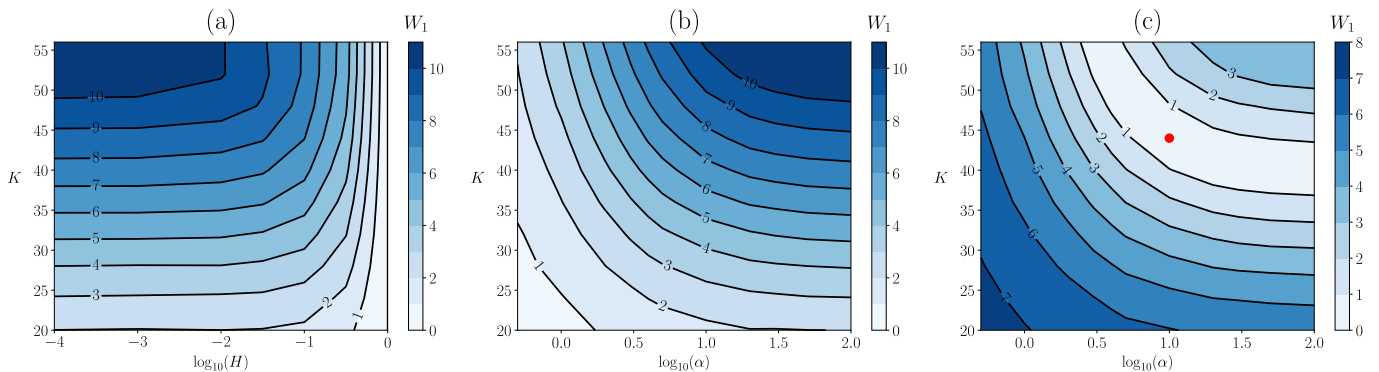


FIG. 5. Illustration of distances $W_1(h_0^{(I)}, h_0^{(II)})$ with (I) and (II) labelling the corresponding point patterns from which persistence diagrams for h_0 (connected components) are computed. In panels (a) and (b), (I) is a random arrangement and (II) is varied with (a) different H and K with $\alpha = 100$ (corresponding to the stealthy HU regime for sufficiently small H), and (b) different α and K with $H = 10^{-4}$. In panel (c), we show the distance from a selected HU pattern: (I) is an arrangement featuring $K = 44\pi$, $H = 10^{-4}$, $\alpha = 10$ and (II) patterns featuring different α and K with $H = 10^{-4}$. The parameter corresponding to the pattern (I) is marked as a red dot.

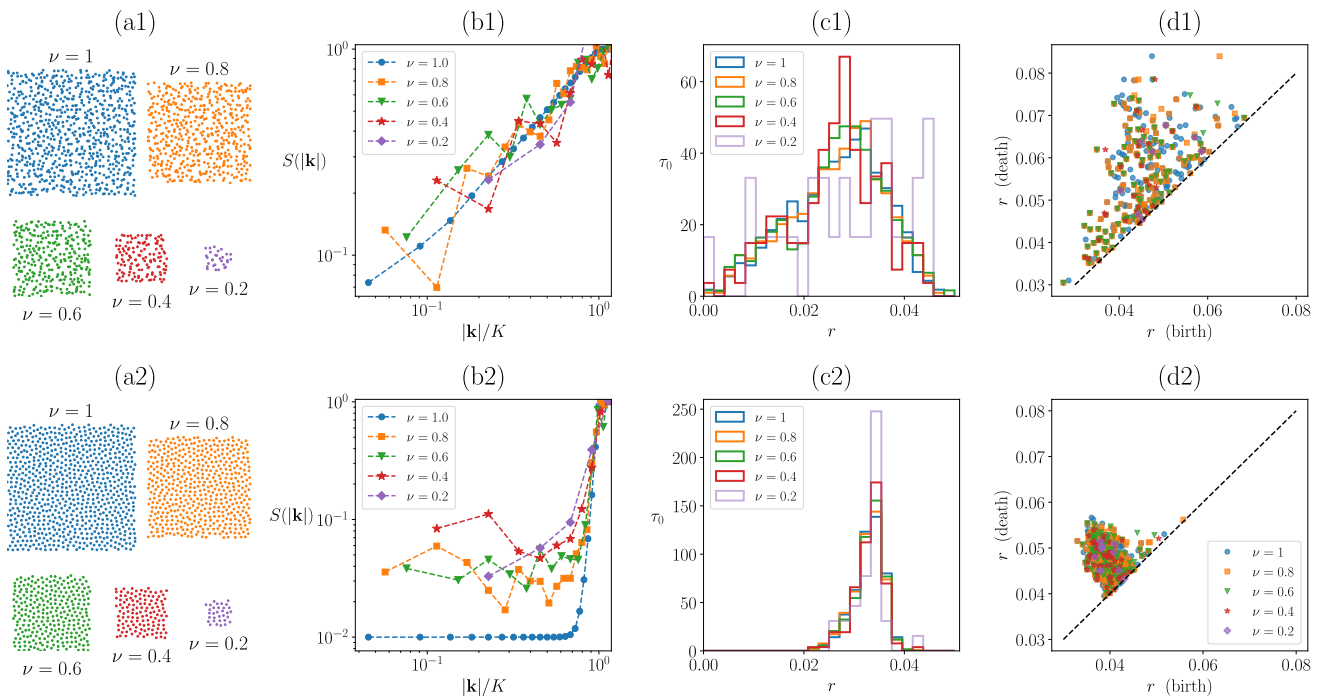


FIG. 6. Topological properties of an ideal HU point pattern are conserved in subsets of that point pattern. (a1)-(a2) Different sets obtained by selecting a $\nu \times \nu$ region of a pattern generated as in the previous section ($\nu = 1$) with $K = 44\pi$, $H = 10^{-2}$, (a1) $\alpha = 1$ and (a2) $\alpha = 20$. For these patterns we show: (b1)-(b2) $S(|k|)$, (c1)-(c2) histograms τ_0 (d1)-(d2) h_1 persistence diagrams.

to compare persistence diagrams or related barcodes are summarized in [58].

Figure 5 illustrates W_1 between h_0 (connected components) persistence diagrams of a random pattern and patterns obtained by varying (a) H and K with $\alpha = 100$ and (b) α and K with $H = 10^{-4}$, both featuring stealthy HU configurations for sufficiently small H and large α . The qualitative trends emerging in Fig. 2 are quantified by W_1 , showing that, as K and α increase, the pattern

becomes less similar to a random pattern, whereas when H increases the pattern looks more like a random pattern, Fig. 5. From these results, we see that the topological properties of the ideal limit $H \sim 0$ are effectively obtained for $H < 10^{-3}$ (see, Fig. 5a). No further effects are expected by lowering H below 10^{-4} for the domain size and number of points considered here. This is a useful estimation as H quantifies HU character in realistic settings: in a system with hundreds of points, we find

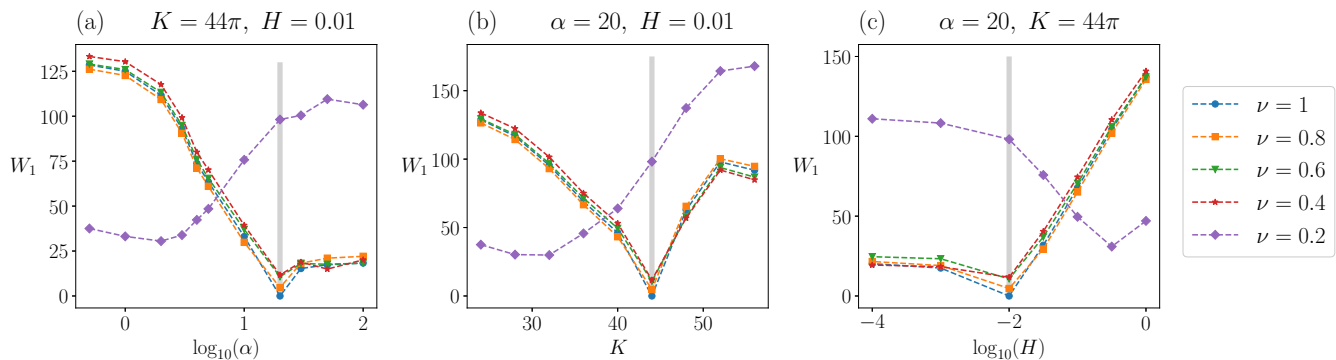


FIG. 7. Topological properties of finite subsets of a HU point pattern are closest to reference patterns generated with the same parameters. We compute $W_1(\tau_0^{(I)}, \tau_0^{(II)})$ with (I) the patterns in Fig. 6(a2) and (II) reference arrangements generated with different $S(|\mathbf{k}|)$ parameters, averaged over ten numerical realizations. Different panels show variation of one parameter, namely (a) α , (b) K , (c) H , while others are held constant for values specified in the figure. Vertical grey lines show the actual value used to generate the subset data Fig. 6(a2).

that $H < 10^{-3}$ leads to topologies sufficiently similar to the ones of ideal HU point clouds. Similar results are obtained with W_2 between persistence diagrams for h_0 ; see Supplemental Material. Distances (both W_1 and W_2) between persistence diagrams for h_1 (holes) follow similar trends for a broad range of K and α values. However, distances from random patterns slightly decrease for increasingly large values of K and α (ordered systems). Thus, comparing h_1 is somewhat less effective at characterizing topological differences than comparing h_0 .

Alternatively, we can measure the distance of persistent diagrams to a reference one obtained for a HU arrangement. This is illustrated in Fig. 5c, which shows W_1 between h_0 (connected components) persistence diagrams of a reference configuration corresponding to a pattern obtained with $K = 44\pi$, $\alpha = 10$ and $H = 10^{-4}$ (red dot in Fig. 5c), and ones obtained by varying α and K . W_1 generally increases when moving towards random (small K and α) or ordered (large K and α) arrangements. Interestingly, a vanishing distance is obtained for the reference configuration (at the red dot) as well as along a curve in the K - α parameter space passing through this point. Analogous topological properties are thus obtained with different parameter combinations for $S(\mathbf{k})$. Said otherwise, there exists a manifold in the parameter space where patterns possess analogous topological properties. The same conclusion can be drawn from W_2 and h_1 (holes) persistent diagrams; see Supplemental Information. This concept will be explored further in section IV.

We now investigate how the structure factor and topological properties are affected by finite-sized data. We consider two specific arrangements of points generated as above with $H = 10^{-2}$, a nearly-HU pattern, and $K = 44\pi$, $\alpha = 1$ as well as $K = 44\pi$, $\alpha = 20$, resulting in visually distinct point patterns, Fig. 6a1-a2. We select points within $\nu \times \nu$ squares of different sizes with $\nu \leq 1$ ($\nu = 1$ is the original arrangement), see Fig. 6a. Whilst

the structure factor $S(\mathbf{k})$ matches the desired S_0 at $\nu = 1$ by construction, for subsets $\nu < 1$ it deviates from that of the full data ($\nu = 1$), Fig. 6b1-b2. These subsets, which are not periodic and mimic realistic data where only a portion of the system can be analyzed, highlight the issue with characterizing HU arrangements by an inferred $S(\mathbf{k})$. Instead, we leverage topological features to assess how similar a finite-size pattern is to an ideally generated HU arrangement. For instance, one may look at the normalized histograms τ_0 (death times of connected components), see Fig. 6c1-c2. These distributions have a similar shape for $\nu \geq 0.4$, pointing at some robust topological properties only deviating for small ν ($\nu = 0.2$). Similarly, the persistence diagrams for h_1 (holes) appears conserved across ν , Fig. 6d1-d2.

To quantitatively assess the extent to which topological properties, here τ_0 , are conserved for finite-sized data, we computed the W_1 distance between the τ_0 distribution of the five patterns in Fig. 6a2 and reference ideal patterns generated by varying separately α , K , H , see Fig. 7. The reference distribution was created using ten simulated repetitions for each ideal pattern. The finite-sized data was closest to the correct reference parameters in all cases for $\nu \geq 0.4$, Fig. 7. The minimum distance obtained for the smallest subset ($\nu = 0.2$) deviates significantly due to the extremely small number of points, reflecting a statistical lower bound on the size of the point set required to correctly identify its topological features. Consistent with observations reported above, using W_2 also finds that the finite-sized patterns are closest to the correct reference pattern for $\nu \geq 0.4$.

We conclude that topological properties of point patterns set by an ideal $S(\mathbf{k})$ are still present in subsets of the same arrangements. In this case, we compared distributions of τ_0 with a W_1 distance as an example, but other topological features or distances can be used.

IV. TOPOLOGICAL STRUCTURE OF NEIGHBORHOODS

Beyond the topological features of connected components and loops (persistent homology), we now examine the related [59] topological structure of neighborhoods [48, 49, 60, 61]. Given a point pattern, we start from the corresponding Delaunay triangulation, dual of the Voronoi diagram, a topological object connecting neighboring points [46]. The Delaunay triangulation will be different for each realization of a point pattern. Still, by capturing its statistical properties, we can examine how the topology of neighborhoods systematically changes across different generating procedures.

We use a recently introduced framework that statistically characterizes the local structure of the Delaunay triangulation and allows physically interpretable comparisons between different point patterns [48, 49]. Starting from the Delaunay triangulation, interpreted as a planar graph, for each vertex of this graph, we take the local *neighborhood* of radius r_g ; the induced subgraph formed by the set of all vertices which are at most r_g edges away from the central vertex, Fig. 8a. We use $r_g = 2$ for computational and statistical purposes, which still results in tens of thousands of unique local neighborhoods [48]. Two local neighborhoods are the same topological type, or *motif*, if they are graph-isomorphic. We characterize the topo-statistical state of a point pattern M as a probability distribution over the space of these motifs, where $P_M(i)$ is the probability of seeing motif i .

Delaunay triangulations are invariant under infinitesimal perturbation and change only through discrete topological transitions, Fig. 8b. A natural distance between two motifs is then the minimum number of topological transitions required to transform one into the other, Fig. 8c, a mathematically well-defined metric [62]. Given two probability distributions P_A and P_B corresponding to different classes of point patterns, a natural distance between A and B is to measure how many transitions are required to transform distribution P_A into P_B . Mathematically, this is a Wasserstein distance, known as a topological earth mover’s (TEM) distance

$$\text{TEM}(A, B) = \min_{\gamma} \sum_{ij} \gamma_{ij} d(i, j), \quad (11)$$

with $d(i, j)$ the distance between motifs i and j and γ_{ij} a transport map from A to B ($\gamma_{ij} \geq 0$, $\sum_j \gamma_{ij} = P_A(i)$, and $\sum_i \gamma_{ij} = P_B(j)$), which can be solved as a minimum cost flow problem on a network, Fig. 8d. Interpreting each transition as having an energetic cost associated with it, the distance $\text{TEM}(A, B)$ can be interpreted as the average overall energetic cost to transform A into B .

Taking different point patterns generated by varying α , K , and that are effectively HU ($H < 10^{-3}$), we computed the pairwise distance between each of them, resulting in an $np \times np$ distance matrix \mathcal{D} , where np is the overall number of unique parameters. To visualize this

matrix, we find a low dimensional embedding with Multi-Dimensional Scaling (MDS) [63], which finds the most faithful way to embed points in Euclidean space while matching the embedded Euclidean distances to the distance matrix \mathcal{D} . Interestingly, we find that in the embedded area, the data falls on an effectively one-dimensional manifold, Fig. 9a, despite us varying two independent parameters (to quantify manifold dimensionality see Supplementary Material). We see a systematic trend on varying either α or K , where increasing either parameter moves us from the disordered side of the manifold (positive Principal Component 1) towards the ordered side of the manifold (negative Principal Component 1).

Generically, when varying m parameters, one expects a m -dimensional data manifold, yet our effectively one-dimensional manifold means that topologically similar patterns can be obtained with different values in parameter space. This is consistent with our finding in Fig. 5c, that there is a region of $\alpha - K$ parameter space at zero (or very small) W_1 distance from a given HU reference arrangement, suggesting that fewer than two parameters are needed to specify the topological features.

To test this property further, we consider another parametrization of S_0 , which differs from the previous power-law definition, namely,

$$S_0^T = H + (1 - H) \frac{1}{2} \left[1 - \tanh \left(\frac{3(K' - |\mathbf{k}|)}{\alpha' \pi} \right) \right], \quad (12)$$

with K' and α' auxiliary parameters mimicking the role K and α in Eq. (6) (the same names without “prime” will be used in the following). Combining new point patterns with this modified parameterization, we calculate an expanded distance matrix and once again embed it in a low-dimensional space with MDS. The data still lies on a one-dimensional manifold, Fig. 9b, showing that this is not just a property emerging from a particular form for S_0 . Indeed, the space of topological neighborhoods for these HU point patterns appears to be one-dimensional, which is not a generic property of 2D point patterns [48].

Looking at the manifold, or curve, we see that it is not a straight line in the embedding. This means that the path taken along the curve is not optimal with respect to the number of topological transitions. Alternatively said, if one were to take an optimal path from, say $K = 20\pi$, $\alpha = 0.5$ to $K = 56\pi$, $\alpha = 100$, then intermediate points on this path would not lie on the 1D manifold. The manifold appears to be maximally distorted for values of Principal Component 1 greater than zero. Still, one can not judge this solely by eye due to inherent distortions that occur when embedding a distance matrix in a low-dimensional Euclidean space.

Instead, we can turn to metric geometry to quantify how far from optimal the manifold path is without resorting to Euclidean embeddings. In plane geometry, three points, A , B , and C , uniquely define a circle. If those points lie on a curve, in the limit that $A, C \rightarrow B$, the circle converges, and the inverse radius of the limiting circle defines the curvature at B . The Menger curvature

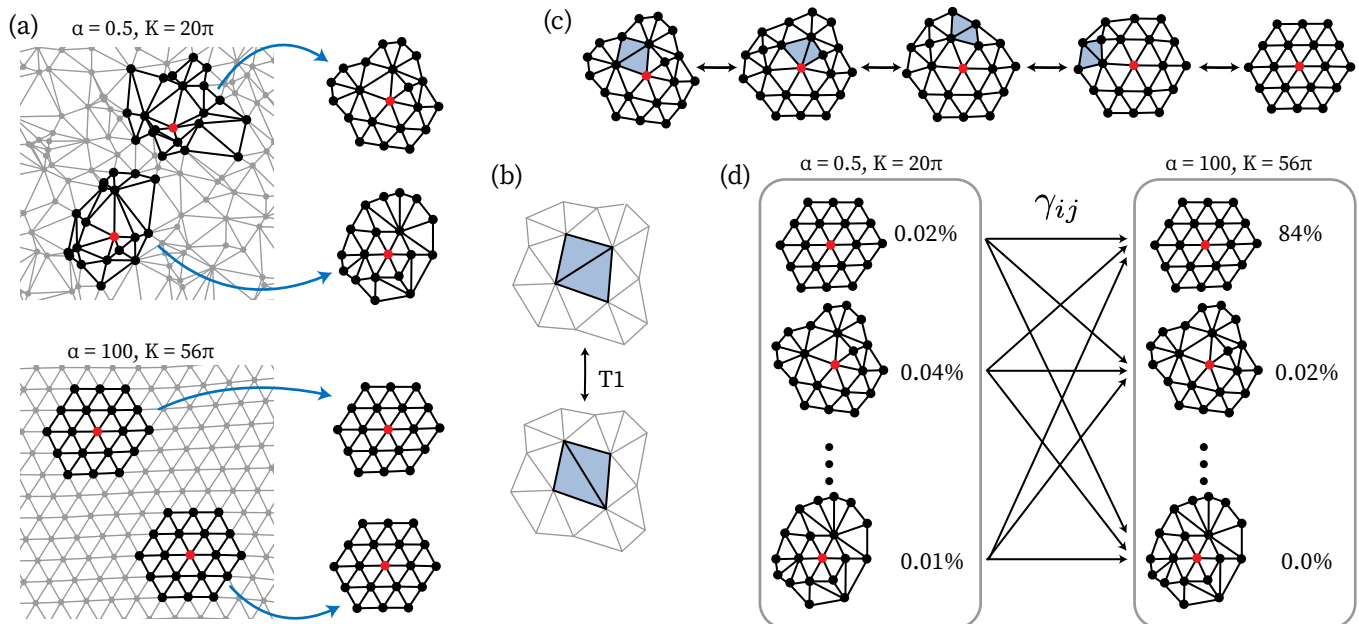


FIG. 8. Comparing two HU patterns based on the distribution of local topological networks or motifs. (a) Starting from a HU point pattern, shown for two parameter values ($\alpha = 0.5$, $K = 20\pi$, top and $\alpha = 100$, $K = 56\pi$, bottom), we take the Delaunay tessellation. The local network of radius $r = 2$ is the subgraph induced by neighbors and nearest neighbors around a central vertex; four examples are shown in black with a red central vertex. (b) The Delaunay tessellation is a topological object and only changes through discrete T1 transitions or flips. (c) Any motif can be transformed into any other motif through a finite sequence of flips. The motif on the left is transformed into the motif on the right with as few flips as possible. The triangles to be flipped as one moves to the right are shown in blue. (d) For a given HU point pattern, there is a probability distribution of local motifs, each occurring with some frequency; to compare two HU patterns, we compare these distributions. We do this by solving an optimal transport problem, finding a transport map γ between two distributions, with the cost of transforming motif i to j set by the number of flips to transform one motif into the other. In effect, the distance represents the minimal number of flips needed to transform the left distribution into the right one.

is the curvature defined by this procedure, but which calculates the radius of the circle using only the distances AB , AC , and BC , Fig. 9c. This definition can then be extended to compute curvatures for any metric space, not just Euclidean ones, as it only uses distances. This allows us to quantify curvature along a 1D manifold in the topological space without ever embedding it into a lower-dimensional Euclidean space.

We can compute the Menger curvature at each point by parameterizing the 1D embedding manifold by a single parameter t , say the position along PC 1. As an aside, we could add new HU or non-HU patterns to the embedding and compute their value of t , finding where they lie along the manifold or whether they lie away from the manifold. Given the parameterization, t , we use a Gaussian kernel density estimator with width σ to approximate a continuous probability distribution $p_t(i)$ for motif index i . The curvature can be computed from this by effectively regularizing the distance into a space with a unique geodesic [48, 49]. We find that the curvature is indeed smallest in the region corresponding to more ordered HU configurations and largest when approaching the region of disordered arrangements, Fig. 9d. Interestingly, the curvature is always non-zero, reflecting that the path taken is not optimal. If our samples effectively

span the space of HU patterns, then the curved nature of the manifold means that to get from one HU pattern to another, either you have to transition through a non-HU pattern or the path taken is not optimal with respect to neighborhood rearrangements.

V. CONCLUSIONS

In summary, by looking at the topological properties of HU configurations we can characterize and study their features in a way that is orthogonal to the structure factor. The persistence diagrams differentiate HU patterns across a wide range of parameters. Moreover, distributions of topological properties are approximately conserved for finite-sized patterns. This enables the matching of these properties from a finite pattern, arising for instance from an experiment, to that of a reference ideal configuration. This approach can complement the characterization of hyperuniformity with classical tools when directly estimating the structure factor is challenging. Additionally, we analyzed the topological structure of local neighborhoods, comparing point patterns through a topological earth mover's distance, which measures the

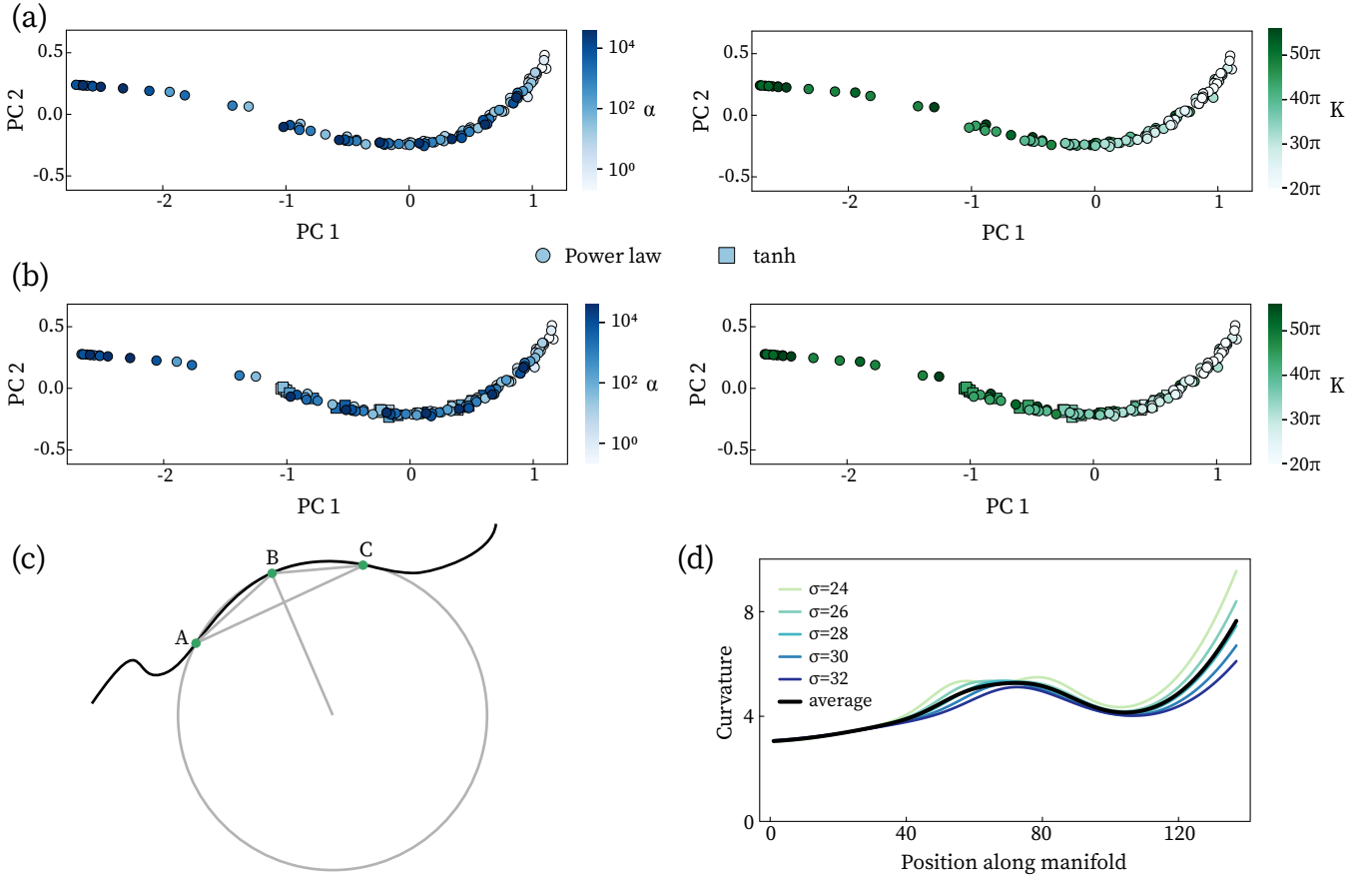


FIG. 9. Across a 2D region of parameter values, the resulting HU patterns lie on a nearly 1D manifold in a low dimensional embedding. (a) HU patterns were created for a range of α (left) and K (right) parameter values for a power law S_0 . The pairwise topological distance matrix was computed, which then was embedded into Euclidean space with MDS, resulting in an approximately 1D manifold when plotting the first two Principal Components (PCs); see Fig. S8 in the Supplementary Material for PC3 and a residual variance analysis. (b) To test whether the manifold in (a) resulted from the specific power law form of S_0 , we included patterns obtained with a tanh function, S_0^T . Including these additional patterns did not change the form of the embedding. (c) For three points, A , B , and C (green) on an arbitrary curve (black), there is a unique circle that intersects those points (grey), with some radius R and curvature $1/R$, which can be computed by knowing only the pairwise distances between A , B , and C . In the limit that $A, C \rightarrow B$, the limit of the curvature $1/R$ is the Menger curvature, a definition that can be extended to an arbitrary metric space. (d) Menger curvature as a function of position along the manifold in (b). Shown for different KDE widths, σ , as well as the average value.

number of rearrangements needed to go from one pattern to another. This also robustly identifies differences between topological properties in HU patterns.

Both distances between local graph-neighborhood motifs distributions and persistence diagrams show that different parameters used for the generation can lead to similar topological properties. Indeed, when varying two parameters in the structure factor, there was a one-dimensional curve along which (h_0 and h_1) persistence diagrams were equivalent under both the W_1 and W_2 distance (Fig. 5 and Supplemental Material). Similarly, in the space of distribution of local motifs, patterns generated by varying two parameters lie along a one-dimensional curve (Fig. 9). The latter analysis leads to the same results after including patterns generated

with different forms of the structure factor. On the one hand, this result points out that there is no unique correspondence between a structure factor parametrization and the resulting topological features, with important implications for inverse design. On the other hand, this demonstrates that one can control distinctive topological properties by varying *one* effective parameter.

By analyzing the curvature of the 1D manifold in the space of distributions of local motifs [48], we show that the variation of topological properties along the manifold does not correspond to the solution of a topological optimal transport problem. In other words, a system that transitions between different HU states may need to explore topologies that differ from characteristics of HU patterns or take a non-optimal path. Besides its theo-

retical relevance, this result could be used to interpret the emergence of HU states and the transition between HU and non-HU states in systems far from equilibrium [16, 64].

The analysis provided here for prototypical HU point clouds can be straightforwardly extended to patterns featuring different kinds of correlated disorder, such as in disordered lattices [13, 65] or colloidal particles systems with clustering effects [10, 66, 67]. Moreover, an interesting question suggested by this work is whether finite, and ultimately experimental, patterns could be designed based on their topological properties rather than imposing directly the HU condition, which is not defined for finite systems. One could eventually explore their physical properties, for instance their interaction with light, and connect them to specific topological features. Further, our approach, characterizing local topological properties, could be used to investigate local effects of boundaries in finite size or experimental systems [68]. We remark that closing the gap with experimental systems would involve extending the analysis from point patterns to a broader class of HU patterns, such as HU heterogeneous media

and scalar fields, which are also amenable to a topological analysis.

ACKNOWLEDGEMENTS

We thank Marco Abbarchi for useful discussions and valuable comments on the manuscript. M.S. acknowledges support from the German Research Foundation (DFG) within the Research Training Group GRK 2868 D³ - project number 493401063. D.J.S. acknowledges NSF Award DMS-1764421 with Simons Foundation grant 597491. A.V. acknowledges the German Research Foundation under Germany's Excellence Strategy, EXC-2068-390729961, Cluster of Excellence Physics of Life at TU Dresden. The authors also gratefully acknowledge computing time granted by the Center for Information Services and High-Performance Computing [Zentrum für Informationsdienste und Hochleistungsrechnen (ZIH)] at TU Dresden and the MIT SuperCloud and Lincoln Laboratory Supercomputing Center.

-
- [1] S. Torquato and F. H. Stillinger, Local density fluctuations, hyperuniformity, and order metrics, *Phys. Rev. E* **68**, 041113 (2003).
 - [2] S. Torquato, Hyperuniform states of matter, *Physics Reports* **745**, 1 (2018).
 - [3] S. Yu, C.-W. Qiu, Y. Chong, S. Torquato, and N. Park, Engineered disorder in photonics, *Nat. Rev. Mater.* **6**, 226 (2021).
 - [4] R. L. Jack, I. R. Thompson, and P. Sollich, Hyperuniformity and phase separation in biased ensembles of trajectories for diffusive systems, *Phys. Rev. Lett.* **114**, 060601 (2015).
 - [5] M. Skolnick and S. Torquato, Simulated diffusion spreadability for characterizing the structure and transport properties of two-phase materials, *Acta Mater.* **250**, 118857 (2023).
 - [6] J. H. Weijs, R. Jeanneret, R. Dreyfus, and D. Bartolo, Emergent hyperuniformity in periodically driven emulsions, *Phys. Rev. Lett.* **115**, 108301 (2015).
 - [7] Y. Zheng, L. Liu, H. Nan, Z.-X. Shen, G. Zhang, D. Chen, L. He, W. Xu, M. Chen, Y. Jiao, and H. Zhuang, Disordered hyperuniformity in two-dimensional amorphous silica, *Sci. Adv.* **6**, eaba0826 (2020).
 - [8] M. Salvalaglio, M. Bouabdellaoui, M. Bollani, A. Benali, L. Favre, J.-B. Claude, J. Wenger, P. de Anna, F. Intonti, A. Voigt, *et al.*, Hyperuniform monocrystalline structures by spinodal solid-state dewetting, *Phys. Rev. Lett.* **125**, 126101 (2020).
 - [9] G. Zhang, F. H. Stillinger, and S. Torquato, The perfect glass paradigm: Disordered hyperuniform glasses down to absolute zero, *Sci. Rep.* **6**, 36963 (2016).
 - [10] W. Wang, R. Díaz-Méndez, M. Wallin, J. Lidmar, and E. Babaev, Pinning effects in a two-dimensional cluster glass, *Phys. Rev. B* **104**, 144206 (2021).
 - [11] S. Mitra, A. D. S. Parmar, P. Leishangthem, S. Sastry, and G. Foffi, Hyperuniformity in cyclically driven glasses, *J. Stat. Mech.: Theory Exp.* **2021** (3), 033203.
 - [12] Q. Le Thien, D. McDermott, C. J. O. Reichhardt, and C. Reichhardt, Enhanced pinning for vortices in hyperuniform pinning arrays and emergent hyperuniform vortex configurations with quenched disorder, *Phys. Rev. B* **96**, 094516 (2017).
 - [13] J. B. Llorens, I. Guillamón, I. G. Serrano, R. Córdoba, J. Sesé, J. M. De Teresa, M. R. Ibarra, S. Vieira, M. Ortuño, and H. Suderow, Disordered hyperuniformity in superconducting vortex lattices, *Phys. Rev. Res.* **2**, 033133 (2020).
 - [14] J. A. Sánchez, R. C. Maldonado, M. L. Amigó, G. Nieva, A. Kolton, and Y. Fasano, Disordered hyperuniform vortex matter with rhombic distortions in fese at low fields, *Phys. Rev. B* **107**, 094508 (2023).
 - [15] Y. Jiao, T. Lau, H. Hatzikirou, M. Meyer-Hermann, J. C. Corbo, and S. Torquato, Avian photoreceptor patterns represent a disordered hyperuniform solution to a multiscale packing problem, *Phys. Rev. E* **89**, 022721 (2014).
 - [16] M. Huang, W. Hu, S. Yang, Q.-X. Liu, and H. Zhang, Circular swimming motility and disordered hyperuniform state in an algae system, *Proc. Natl. Acad. Sci. U.S.A.* **118**, e2100493118 (2021).
 - [17] A. Gabrielli, M. Joyce, and F. Sylos Labini, Glass-like universe: Real-space correlation properties of standard cosmological models, *Phys. Rev. D* **65**, 083523 (2002).
 - [18] A. Gabrielli, B. Jancovici, M. Joyce, J. L. Lebowitz, L. Pietronero, and F. Sylos Labini, Generation of primordial cosmological perturbations from statistical mechanical models, *Phys. Rev. D* **67**, 043506 (2003).
 - [19] Y. A. Gerasimenko, I. Vaskivskiy, M. Litskevich, J. Ravnik, J. Vodeb, M. Diego, V. Kabanov, and D. Mihailovic, Quantum jamming transition to a correlated elec-

- tron glass in 1t-tas2, *Nat. Mater.* **18**, 1078 (2019).
- [20] R. Degl'Innocenti, Y. Shah, L. Masini, A. Ronzani, A. Pianti, Y. Ren, D. Jessop, A. Tredicucci, H. Beere, and D. Ritchie, Hyperuniform disordered terahertz quantum cascade laser, *Sci. Rep.* **6**, 19325 (2016).
- [21] L. S. Froufe-Pérez, M. Engel, J. J. Sáenz, and F. Scheffold, Band gap formation and anderson localization in disordered photonic materials with structural correlations, *Proc. Natl. Acad. Sci. U.S.A.* **114**, 9570 (2017).
- [22] Z. Chehadi, M. Bouabdellaoui, M. Modaresialam, T. Bottein, M. Salvalaglio, M. Bollani, D. Grosso, and M. Abbarchi, Scalable disordered hyperuniform architectures via nanoimprint lithography of metal oxides, *ACS Appl. Mater. Interfaces* **13**, 37761 (2021).
- [23] K. Vynck, R. Pacanowski, A. Agreda, A. Dufay, X. Granier, and P. Lalanne, The visual appearances of disordered optical metasurfaces, *Nat. Mater.* **21**, 1035 (2022).
- [24] N. Granchi, M. Lodde, K. Stokkerei, R. Spalding, P. J. van Veldhoven, R. Sapienza, A. Fiore, M. Gurioli, M. Florescu, and F. Intonti, Near-field imaging of optical nanocavities in hyperuniform disordered materials, *Phys. Rev. B* **107**, 064204 (2023).
- [25] K. Vynck, R. Pierrat, R. Carminati, L. S. Froufe-Pérez, F. Scheffold, R. Sapienza, S. Vignolini, and J. J. Sáenz, Light in correlated disordered media, *Rev. Mod. Phys.* **95**, 045003 (2023).
- [26] N. P. Mitchell, L. M. Nash, D. Hexner, A. M. Turner, and W. T. Irvine, Amorphous topological insulators constructed from random point sets, *Nat. Phys.* **14**, 380 (2018).
- [27] Y. Xu, S. Chen, P.-E. Chen, W. Xu, and Y. Jiao, Microstructure and mechanical properties of hyperuniform heterogeneous materials, *Phys. Rev. E* **96**, 043301 (2017).
- [28] S. Ghosh and J. Lebowitz, Number rigidity in superhomogeneous random point fields, *J. Stat. Phys.* **166**, 1016 (2017).
- [29] M. A. Klatt, J. Lovrić, D. Chen, S. C. Kapfer, F. M. Schaller, P. W. A. Schönhöfer, B. S. Gardiner, A.-S. Smith, G. E. Schröder-Turk, and S. Torquato, Universal hidden order in amorphous cellular geometries, *Nat. Commun.* **10**, 811 (2019).
- [30] M. A. Klatt and G. Last, On strongly rigid hyperfluctuating random measures, *J. Appl. Prob.* **59**, 948–961 (2022).
- [31] O. U. Uche, F. H. Stillinger, and S. Torquato, Constraints on collective density variables: Two dimensions, *Phys. Rev. E* **70**, 046122 (2004).
- [32] O. U. Uche, S. Torquato, and F. H. Stillinger, Collective coordinate control of density distributions, *Phys. Rev. E* **74**, 031104 (2006).
- [33] M. Florescu, S. Torquato, and P. J. Steinhardt, Designer disordered materials with large, complete photonic band gaps, *Proc. Natl. Acad. Sci. U.S.A.* **106**, 20658 (2009).
- [34] P. K. Morse, J. Kim, P. J. Steinhardt, and S. Torquato, Generating large disordered stealthy hyperuniform systems with ultrahigh accuracy to determine their physical properties, *Phys. Rev. Res.* **5**, 033190 (2023).
- [35] D. Hawat, G. Gautier, R. Bardenet, and R. Lachièze-Rey, On estimating the structure factor of a point process, with applications to hyperuniformity, *Stat. Comput.* **33**, 61 (2023).
- [36] D. Chen, Y. Zheng, and Y. Jiao, Topological defects, inherent structures, and hyperuniformity, *Phys. Rev. B* **104**, 174101 (2021).
- [37] S. Tsabedze, N. Dlamini, and S. K. Mkhonta, Regularity and resilience of short-range order in uniformly randomized lattices, *J. Phys. Commun.* **6**, 105008 (2022).
- [38] J. Puig, J. A. Sánchez, G. Nieva, A. B. Kolton, and Y. Fasano, Hyperuniformity in type-II superconductors with point and planar defects, *JPS Conf. Proc.* **38**, 011051 (2023).
- [39] L. Wasserman, Topological data analysis, *Annu. Rev. Stat. Appl.* **5**, 501 (2018).
- [40] Edelsbrunner, Letscher, and Zomorodian, Topological persistence and simplification, *Discret. Comput. Geometry* **28**, 511 (2002).
- [41] H. Edelsbrunner, J. Harer, *et al.*, Persistent homology—a survey, *Contemp. Math.* **453**, 257 (2008).
- [42] H. Edelsbrunner and J. L. Harer, *Computational topology: an introduction* (American Mathematical Society, 2010).
- [43] V. Robins and K. Turner, Principal component analysis of persistent homology rank functions with case studies of spatial point patterns, sphere packing and colloids, *Physica D* **334**, 99 (2016).
- [44] N. Otter, M. A. Porter, U. Tillmann, P. Grindrod, and H. A. Harrington, A roadmap for the computation of persistent homology, *EPJ Data Sci.* **6**, 1 (2017).
- [45] M. E. Aktas, E. Akbas, and A. E. Fatmaoui, Persistence homology of networks: methods and applications, *Appl. Netw. Sci.* **4**, 1 (2019).
- [46] F. Aurenhammer, R. Klein, and D.-T. Lee, *Voronoi Diagrams and Delaunay Triangulations*, 1st ed. (World Scientific Publishing Co., Inc., River Edge, NJ, USA, 2013).
- [47] E. A. Lazar, J. Lu, and C. H. Rycroft, Voronoi cell analysis: The shapes of particle systems, *Am. J. Phys.* **90**, 469 (2022).
- [48] D. J. Skinner, B. Song, H. Jeckel, E. Jelli, K. Drescher, and J. Dunkel, Topological metric detects hidden order in disordered media, *Phys. Rev. Lett.* **126**, 048101 (2021).
- [49] D. J. Skinner, H. Jeckel, A. C. Martin, K. Drescher, and J. Dunkel, Topological packing statistics of living and non-living matter, *Sci. Advan.* **9**, eadg1261 (2023).
- [50] S. Torquato, G. Zhang, and F. H. Stillinger, Ensemble theory for stealthy hyperuniform disordered ground states, *Phys. Rev. X* **5**, 021020 (2015).
- [51] S. Torquato, O. U. Uche, and F. H. Stillinger, Random sequential addition of hard spheres in high euclidean dimensions, *Phys. Rev. E* **74**, 061308 (2006).
- [52] J. Kim and S. Torquato, Effect of imperfections on the hyperuniformity of many-body systems, *Phys. Rev. B* **97**, 054105 (2018).
- [53] F. Chazal and B. Michel, An introduction to topological data analysis: fundamental and practical aspects for data scientists, *Front. Artif. Intell.*, **4**, 108 (2021).
- [54] S. Torquato, Diffusion spreadability as a probe of the microstructure of complex media across length scales, *Phys. Rev. E* **104**, 054102 (2021).
- [55] C. Tralie, N. Saul, and R. Bar-On, Ripser.py: A lean persistent homology library for python, *J. Open Source Softw.* **3**, 925 (2018).
- [56] U. Bauer, Ripser: efficient computation of Vietoris-Rips persistence barcodes, *J. Appl. Comput. Topol.* **5**, 391 (2021).
- [57] The GUDHI Project, *GUDHI User and Reference Manual* (GUDHI Editorial Board, 2015).
- [58] D. Ali, A. Asaad, M.-J. Jimenez, V. Nanda, E. Paluzo-Hidalgo, and M. Soriano-Trigueros, A survey of vec-

- torization methods in topological data analysis (2022), [arXiv:2212.09703 \[math.AT\]](#).
- [59] U. Bauer and H. Edelsbrunner, The morse theory of čech and delaunay complexes, *Trans. Am. Math. Soc.* **369**, 3741 (2016).
- [60] E. A. Lazar, J. Han, and D. J. Srolovitz, Topological framework for local structure analysis in condensed matter, *Proc. Natl Acad. Sci. U.S.A.* **112**, E5769 (2015).
- [61] E. A. Lazar, J. K. Mason, R. D. MacPherson, and D. J. Srolovitz, Complete topology of cells, grains, and bubbles in three-dimensional microstructures, *Phys. Rev. Lett.* **109**, 095505 (2012).
- [62] C. L. Lawson, Transforming triangulations, *Discrete Math.* **3**, 365 (1972).
- [63] I. Borg and P. J. Groenen, *Modern multidimensional scaling: Theory and applications* (Springer, 2005).
- [64] R. Backofen, A. Y. A. Altawil, M. Salvalaglio, and A. Voigt, Nonequilibrium hyperuniform states in active turbulence (2023), [arXiv:2311.14959 \[cond-mat.soft\]](#).
- [65] D. A. Keen and A. L. Goodwin, The crystallography of correlated disorder, *Nature* **521**, 303 (2015).
- [66] J. Wang, C. F. Mbah, T. Przybilla, B. Apeleo Zubiri, E. Spiecker, M. Engel, and N. Vogel, Magic number colloidal clusters as minimum free energy structures, *Nat. Commun.* **9**, 5259 (2018).
- [67] K. A. Whitaker, Z. Varga, L. C. Hsiao, M. J. Solomon, J. W. Swan, and E. M. Furst, Colloidal gel elasticity arises from the packing of locally glassy clusters, *Nat. Commun.* **10**, 2237 (2019).
- [68] S. Torquato and F. H. Stillinger, Multiplicity of generation, selection, and classification procedures for jammed hard-particle packings, *J. Phys. Chem. B* **105**, 11849 (2001).

Supplemental Material

Persistent homology and topological statistics of hyperuniform point clouds

Marco Salvalaglio,^{1,2} Dominic J. Skinner,³ Jörn Dunkel⁴, Axel Voigt^{1,2,5}

¹*Institute of Scientific Computing, Technische Universität Dresden, 01062 Dresden, Germany*

²*Dresden Center for Computational Materials Science (DCMS), TU Dresden, 01062 Dresden, Germany*

³*NSF-Simons Center for Quantitative Biology, Northwestern University, 2205 Tech Drive, Evanston, IL 60208, USA*

⁴*Department of Mathematics, Massachusetts Institute of Technology,*

77 Massachusetts Avenue, Cambridge, MA 01239, USA

⁵*Cluster of Excellence Physics of Life, Technische Universität Dresden, 01062 Dresden, Germany*

This supplemental material contains:

- Additional persistent diagrams and τ_0 (death times of connected components) distributions illustrated as in Fig. 4 in the main text – [S-I](#).
- Parameters of the Skew-Normal distribution fitted on the distributions of τ_0 – [S-II](#).
- Distances $W_i(h_j^{(I)}, h_j^{(II)})$ as in Fig. 5 in the main text for $i = 1, 2$ and $j = 0, 1$ – [S-III](#).
- Residual variance as a function of embedding dimension quantifying the manifold dimensionality – [S-IV](#).

S-I. PERSISTENT DIAGRAMS

We report additional results complementing the analysis illustrated in Fig. 4 in the main text. We show point clouds obtained by varying α , K , and H (by keeping the other parameters constant) in Fig. [S1](#), Fig. [S2](#), and Fig. [S3](#), respectively.

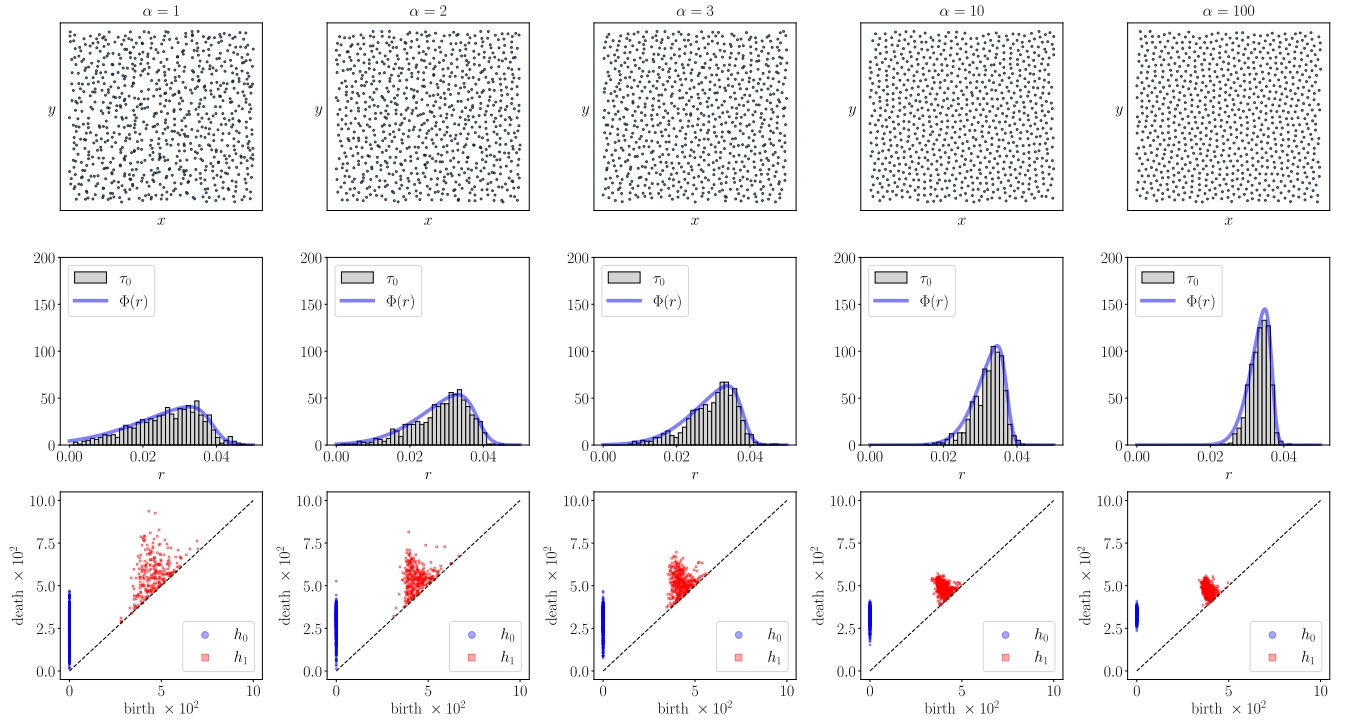


FIG. S1. Point patterns (first row), distribution of τ_0 (death times of connected components) as well as skew-normal distribution fit $\Phi(r)$ (second row), h_0 (connected components) and h_1 (holes) persistent diagrams (third row) varying α for $K = 44\pi$ and $H = 0.01$. See values of α in the first row.

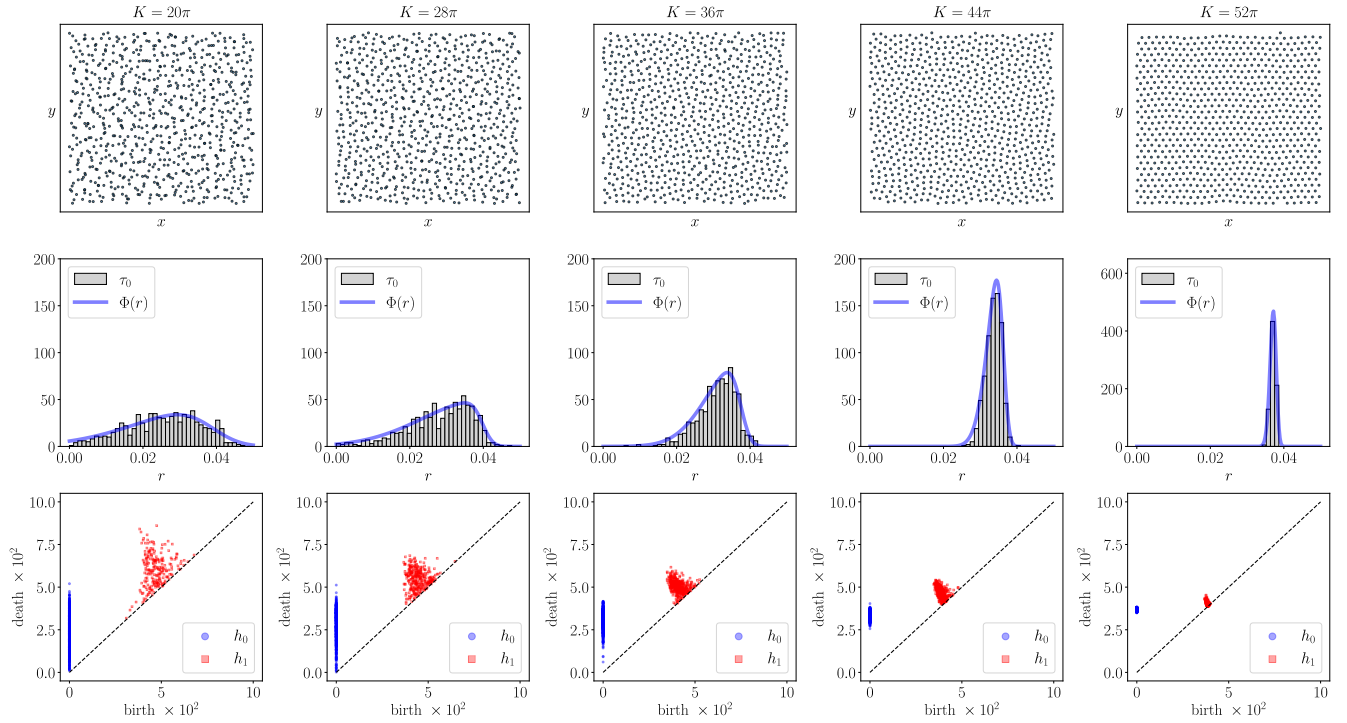


FIG. S2. Point patterns (first row), distribution of τ_0 (death times of connected components) as well as skew-normal distribution fit $\Phi(r)$ (second row), h_0 (connected components) and h_1 (holes) persistent diagrams (third row) varying K for $\alpha = 100$ and $H = 10^{-4}$. See values of K in the first row.

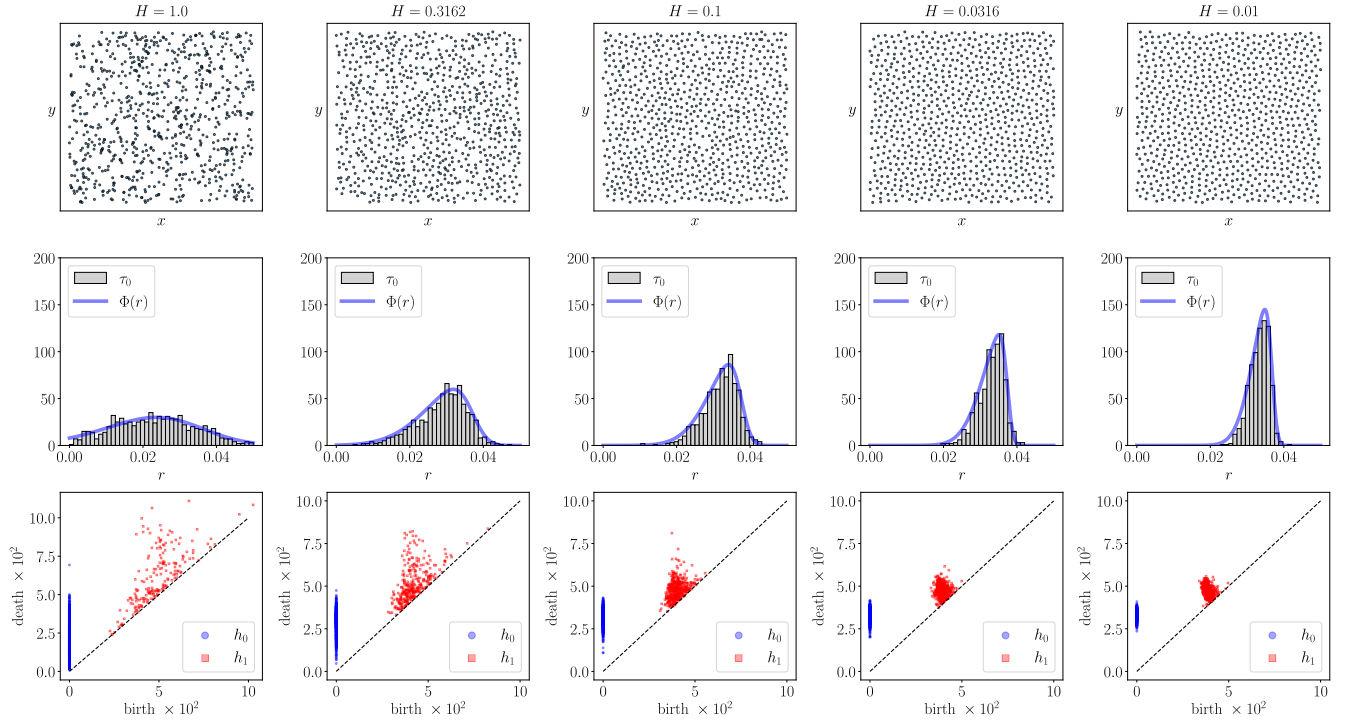


FIG. S3. Point patterns (first row), distribution of τ_0 (death times of connected components) as well as skew-normal distribution fit $\Phi(r)$ (second row), h_0 (connected components) and h_1 (holes) persistent diagrams (third row) varying K for $\alpha = 100$ and $K = 44\pi$. See values of H in the first row.

S-II. PARAMETERS OF THE SKEW-NORMAL DISTRIBUTION

In the main text and Figs. S1–S3, we have shown that the distribution of τ_0 is well described by a skew-normal distribution

$$\Phi(r) = \frac{2}{\omega} \mathcal{N}\left(\frac{r-\mu}{\omega}\right) \mathcal{E}\left(\beta \frac{r-\mu}{\omega}\right), \quad (\text{S1})$$

with

$$\begin{aligned} \mathcal{N}(x) &= \frac{1}{\sqrt{2\pi}} e^{-\frac{x^2}{2}}, \\ \mathcal{E}(x) &= \frac{1}{2} \left[1 + \operatorname{erf}\left(\frac{x}{\sqrt{2}}\right) \right]. \end{aligned} \quad (\text{S2})$$

Fitting parameters ω (the width), μ (the location), and β (the skewness) of the skew-normal distribution for representative patterns are fully illustrated here in Figs. S4–S6. A negative skewness is observed for all the cases. We find ω decreases for increasing α and K for relatively large values of these parameters, quantifying the increase in *uniformity* corresponding to narrower distributions. However, for small α , ω is non-monotonic in K with a finite maximum. μ shows a similar trend, although the value of μ shows limited variation ($\sim 10\%$ across all analyzed cases) as we vary the parameters in the structure factor. The skewness β exhibits an opposite behavior, namely a decrease (increase) of the negative skewness, hence an increase of the distribution asymmetry, for small (large) α and K . For marked HU characters, i.e., large α and K , the observed trend for the skewness results however rather noisy. This may be ascribed to the larger standard deviation accompanying the fitting of the skewness on narrower and narrower distributions.

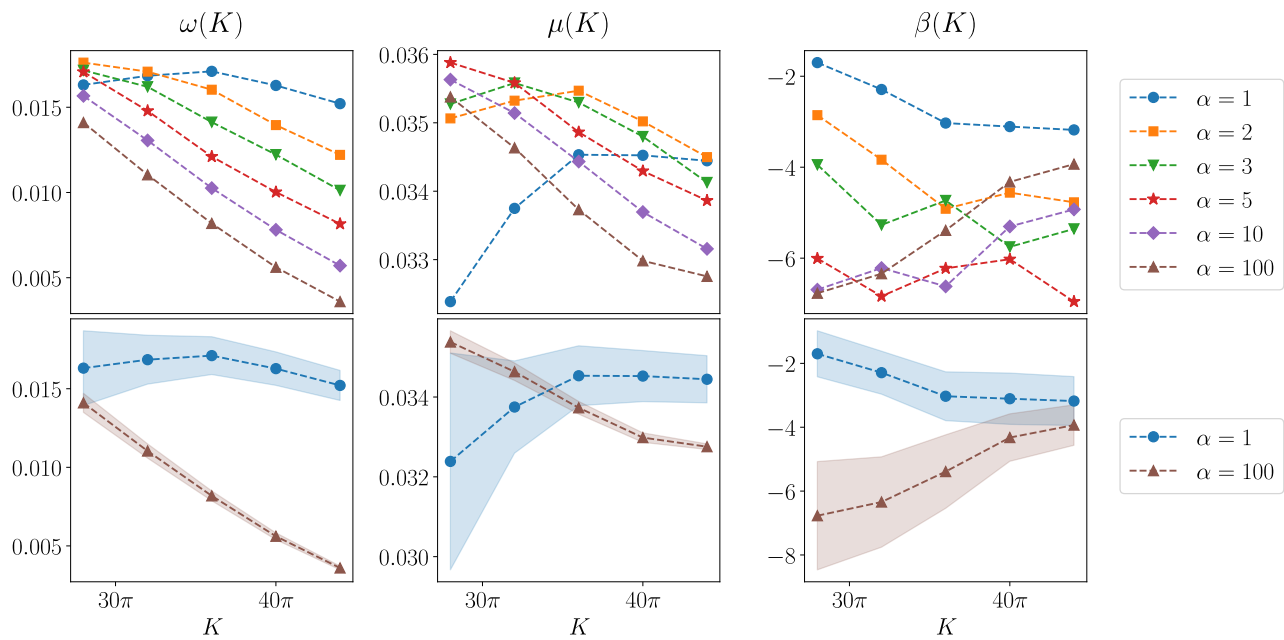


FIG. S4. Parameters of $\Phi(r)$ fitted on the histograms τ_0 by varying K (on the x-axis) and α (different curves), $H = 10^{-4}$. Shaded areas show the 68% confidence intervals.

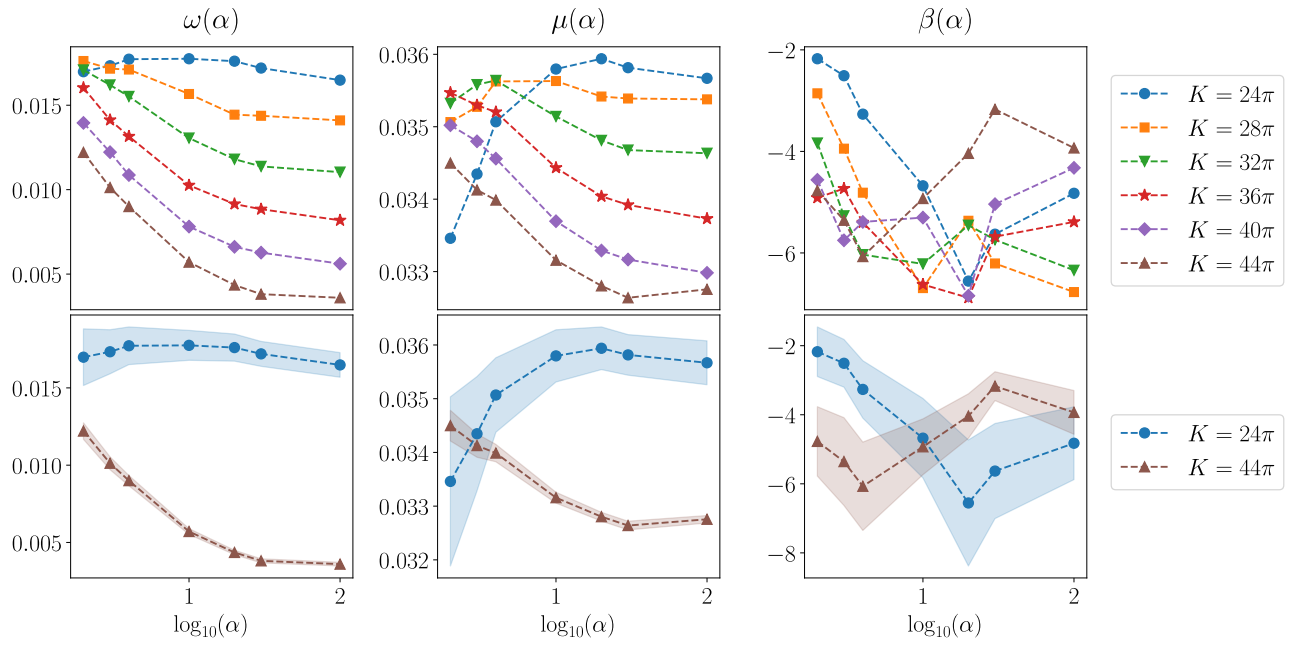


FIG. S5. Parameters of $\Phi(r)$ fitted on the histograms τ_0 by varying α (on the x-axis) for K (different curves), $H = 10^{-4}$. Shaded areas show the 68% confidence intervals.

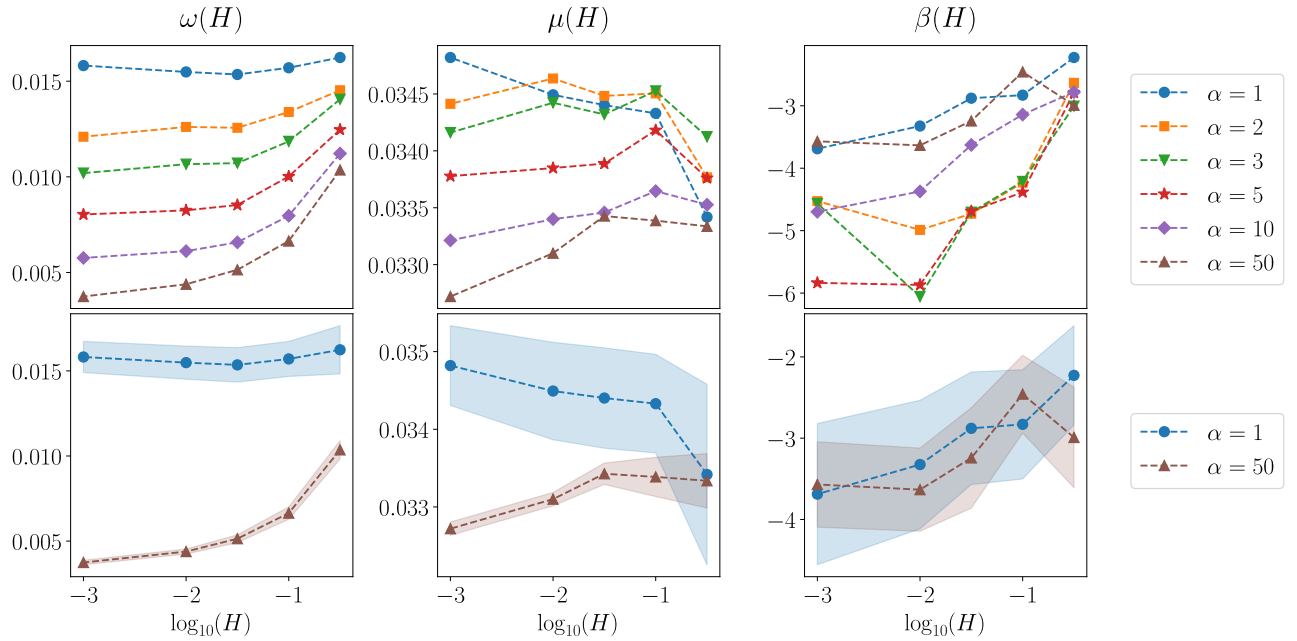


FIG. S6. Parameters of $\Phi(r)$ fitted on the histograms τ_0 by varying H (on the x-axis) and α (different curves), $K = 44\pi$. Shaded areas show the 68% confidence intervals.

S-III. DISTANCES BETWEEN PERSISTENT DIAGRAMS

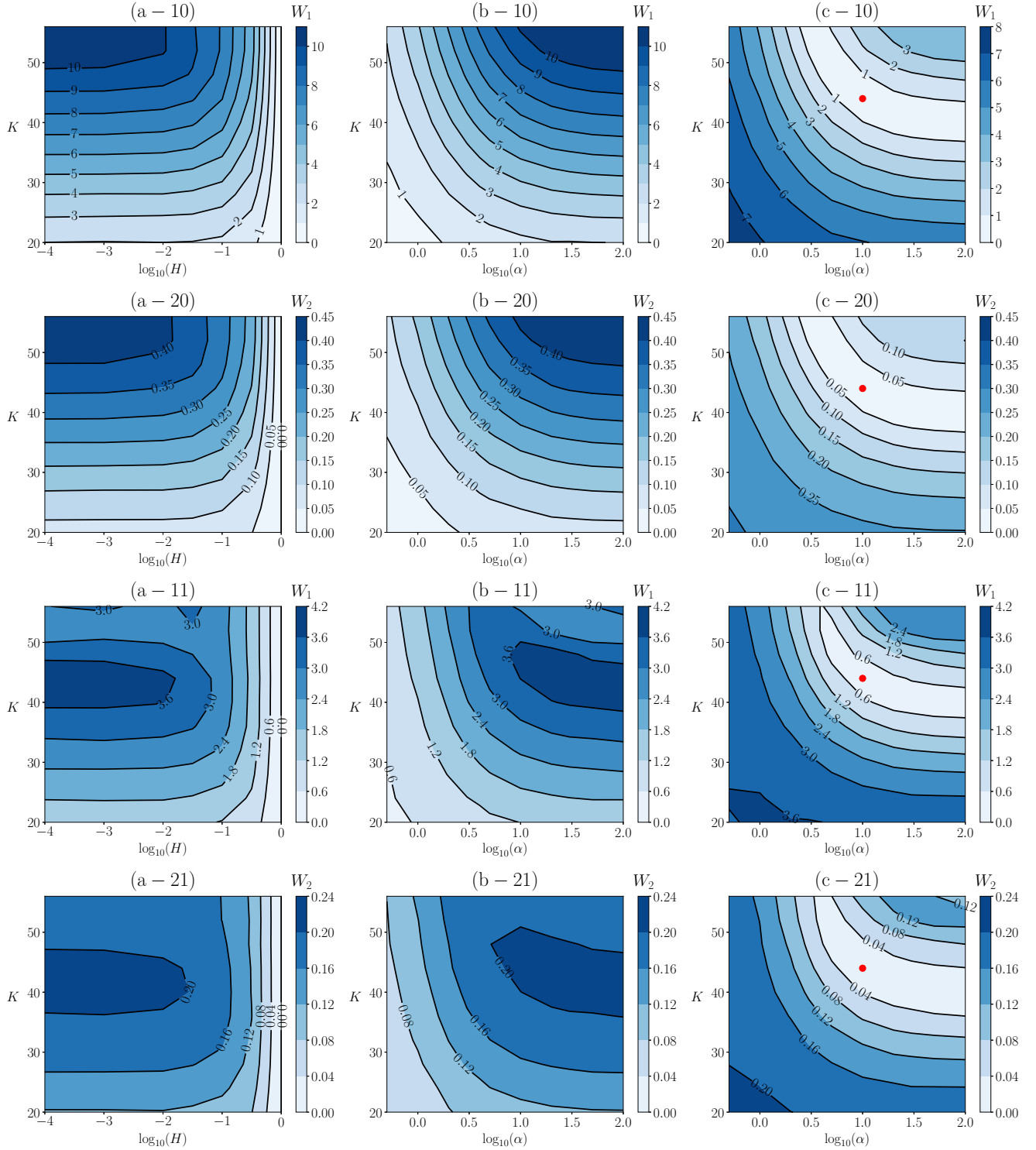


FIG. S7. Illustration of distances $W_i(h_j^{(I)}, h_j^{(II)})$ as in Fig. 5 of the main text with $i = 1, 2$ and $j = 0, 1$. In all columns (I) is held fixed and (II) is varied. In the first and second column (a, b), (I) is a random arrangement. For (II) in the first column, (a), we vary H and K with $\alpha = 100$ (Stealthy HU settings for sufficiently small H). For (II) in the second column, (b), we vary α and K with $H = 10^{-4}$. In the third column (c), (I) is a fixed HU arrangement with $K = 44\pi$, $H = 10^{-4}$, $\alpha = 10$, whereas for (II), we vary α and K with $H = 10^{-4}$. The parameter values corresponding to (I) are marked as a red dot.

S-IV. RESIDUAL VARIANCE

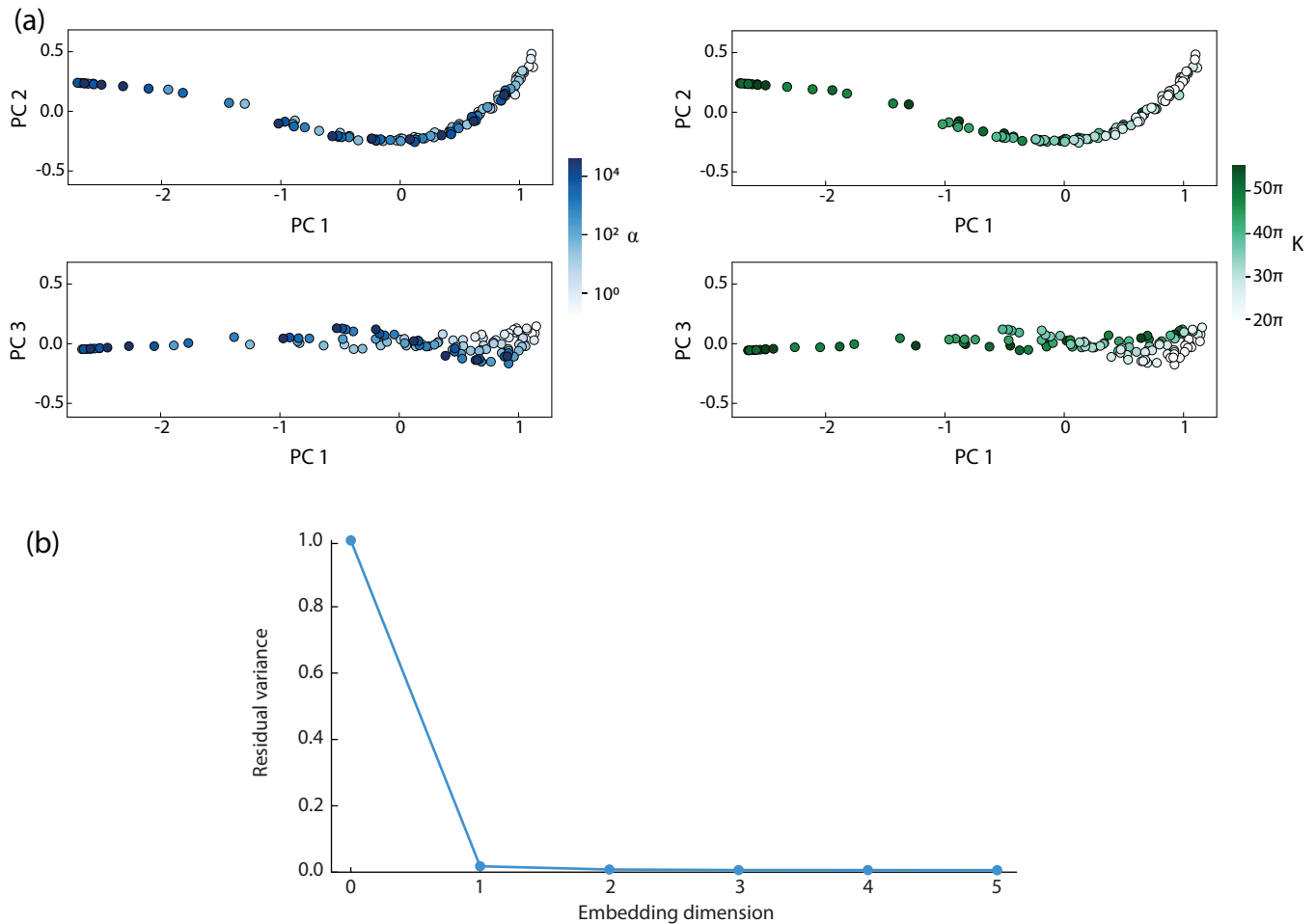


FIG. S8. Quantifying the manifold dimension using the residual variance. (a) MDS embedding of all point patterns across various K and α parameters, for the first three principal components (top is PC1 vs PC2, shown in main text Fig. 9, bottom is PC1 vs PC3). We can see that the manifold is primarily one dimensional and changing either K or α primarily moves a point along the one dimensional curve. For more disordered systems (large PC 1 values), the manifold starts to become more two dimensional with K and α being able to be independently varied. (b) To quantify the dimensionality, we plot the residual variance as a function of embedding dimension. Very little variance remains after a one dimensional embedding, showing the data manifold is essentially one dimensional. Residual variance is defined as $1 - R^2(\mathcal{D}, \hat{\mathcal{D}})$, where \mathcal{D} is the true pairwise distance matrix, $\hat{\mathcal{D}}$ is the Euclidean distance matrix in a low dimensional embedding, and R^2 is the standard correlation coefficient. Here, the low dimensional embedding is an isomap embedding rather than MDS, in order to “unroll” the manifold and find its intrinsic dimension, see Ref. [S1] for details.

[S1] D. J. Skinner, B. Song, H. Jeckel, E. Jelli, K. Drescher, and J. Dunkel, Topological metric detects hidden order in disordered media, *Phys. Rev. Lett.* **126**, 048101 (2021).